Near-Infrared-Absorbing B-N Lewis Pair Functionalized Anthracenes: Electronic Structure Tuning, Conformational Isomerism, and Applications in Photothermal Cancer Therapy

Kanglei Liu*[a,b], Zhenqi Jiang*[b,c], Roger A. Lalancette[a], Xiaoying Tang[c], Frieder Jäkle*[a]

[a] Department of Chemistry, Rutgers University-Newark, 73 Warren Street, Newark, NJ 07102, USA.

[b] Key Laboratory of Cluster Science, Ministry of Education of China, Beijing Key Laboratory of Photoelectronic/Electrophotonic Conversion Materials, School of Chemistry and Chemical Engineering, Beijing Institute of Technology, Beijing 102400, P. R. China.

[c] School of Medical Technology, Beijing Institute of Technology, Beijing 102400, P. R. China.

ABSTRACT: B-N fused dianthracenylpyrazine derivatives are synthesized to generate new low gap chromophores. Photophysical and electrochemical, crystal packing, and theoretical studies have been performed. Two energetically similar conformers are identified by DFT calculations, showing that the core unit adopts a curved saddle-like shape (*x-isomer*) or a zig-zag conformation (*z-isomer*). In the solid state, the *z-isomer* is prevalent according to an X-ray crystal structure of a C_6F_5-substituted derivative (**4-Pf**), but VT NMR studies suggest a dynamic behavior in solution. B-N fusion results in a large decrease of the HOMO-LUMO gap and dramatically lowers the LUMO energy compared to the all-carbon analogs. **4-Pf** in particular shows significant absorbance at greater than 700 nm, while being almost transparent throughout the visible region. After encapsulation in the biodegradable polymer DSPE-mPEG$_{2000}$, **4-Pf-NPs** nanoparticles exhibit good water solubility, high photostability, and excellent photothermal conversion efficiency of ~41.8%. **4-Pf-NPs** are evaluated both *in vitro* and *in vivo* as photothermal therapeutic agents. These results uncover B-N Lewis pair functionalization of PAHs as a promising strategy toward new NIR-absorbing materials for photothermal applications.

INTRODUCTION

Conjugated organic materials play important roles in applications ranging from optoelectronic devices to chemical sensors and imaging.[1] Recently, low gap materials with strong near-infrared (NIR) absorption or emission have gained much interest for use in transparent photovoltaic devices and biomedical imaging applications, where the favorable tissue penetration of NIR light is critically important.[2] In addition, NIR-absorbing organic π-conjugated materials hold great promise as photothermal agents (PTAs) for photothermal therapy (PTT) owing to their favorable biocompatibility, potential biodegradability, high reproducibility, and accessible structure-property relationships.[3] In this respect, the functionalization of π-conjugated systems with main group elements such as boron is attractive because it offers a means to easily tune the electronic structures and optoelectronic properties.[4] Substitution of carbon-carbon (C-C) covalent bonds with isoelectronic dative B←N units has emerged as a versatile strategy to adjust the energy levels and band gap of conjugated materials.[5,6] In addition, the reversibility of the B←N dative bonds in such systems is an attractive feature for development of stimuli-responsive materials and molecular switches.[7] However, so far only a limited number of low gap molecules containing B←N units have been introduced.[8] Further, boron complexes with high photothermal conversion efficiency (PCE) remain very rare and are almost exclusively based on the boron dipyrromethene (BODIPY) scaffold and its derivatives (**A**-**B**, Figure 1).[9]

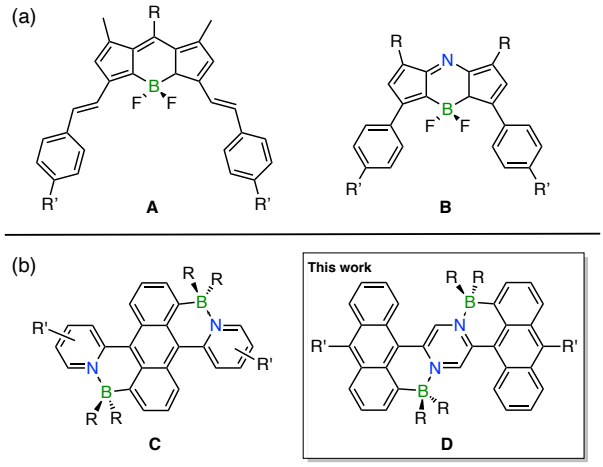

Figure 1. (a) Representative boron complexes applied as photothermal agents and (b) B-N Lewis pair-fused anthracenes as new chromophores.

In 2017, we reported a new class of B-N fused 9,10-dipyridylanthracenes with unique structural features and electronic properties.[10] We found that the formation of B←N Lewis pairs at the periphery of anthracene in compounds **C** (Figure 1) results in dramatically lowered LUMO energy levels, which leads to large bathochromic shifts in the absorption and emis-

sion relative to the all-carbon analogs. These compounds also display very efficient self-sensitized reactivity toward oxygen to form endoperoxides that thermally release singlet oxygen. To achieve a further decrease in the HOMO-LUMO gap of B-N Lewis pair-functionalized anthracenes, and to shift the absorption into the NIR region, we have now designed a new class of borane-modified dianthracenylpyrazines, **D** (Figure 1). We chose pyrazine as a linker because it is an inherently highly electron-deficient heterocycle and binding of boron to pyrazine is known to very effectively lower the LUMO levels, for example, enabling applications as acceptors in organic solar cell applications.[11]

Herein, we demonstrate that the B-N fusion of pyrazine-bridged anthracene dimers **D** generates new conjugated materials with strong acceptor character and absorptions reaching into the NIR region. Both experimental and theoretical studies indicate that compounds **D** exhibit very low-lying LUMO levels and a dramatically decreased HOMO-LUMO gap relative to B-N fused dipyridylanthracenes **C**. Modification of the boryl substituents provides an additional opportunity for LUMO tuning.[6a, 8b, 11h] Thus, the attachment of C_6F_5 electron-withdrawing groups to boron further lowers the HOMO-LUMO gap, offering access to materials that absorb strongly in the NIR. Nanoparticles derived from assembly of **D** (R = C_6F_5) with DSPE-mPEG$_{2000}$ combine a high PCE of 41.8% with excellent stability, both important attributes of effective PTAs. *In vitro* and *in vivo* studies reveal that these nanoparticles give rise to excellent PTT effect with good biosafety in the NIR window. Thus, this study offers a new molecular design concept for the synthesis of NIR-absorbing PTAs.

RESULTS AND DISCUSSION

Synthesis and Structural Characterization of B-N fused dianthracenylpyrazines. The synthetic route to the targeted B-N fused chromophores is shown in Scheme 1 and further details are provided in the Supporting Information (SI). Pd-catalyzed Suzuki-Miyaura coupling of 9,10-bis(pinacolatoboryl)anthrancene (**1**)[12] with 1-bromo-4-*tert*-butylbenzene furnished the unsymmetrically substituted 9-(pinacolatoboryl)-10-(*tert*-butylphenyl)-anthracene (**2**) in 55% yield. *tert*-Butylphenyl groups were introduced to increase the solubility and stability of the final products. Suzuki-Miyaura cross coupling of **2** with dibromopyrazine gave the pyrazine-bridged anthracene dimer **3** in a yield of 59%. Using a protocol first developed by Ingleson,[13] the addition of BCl_3, $AlCl_3$ and the bulky base 2,6-di-*tert*-butylpyridine (DBP) to a DCM solution of **3** resulted in N-directed electrophilic borylation at the 10-position of anthracene to give the fused boracyclic species. Subsequent reaction with $ZnEt_2$ or $Zn(C_6F_5)_2$ produced the targeted B-N doped polycyclic species **4-Et** and **4-Pf** as intensely colored solids. The products are stable in air in the solid state for extended periods of time. The fluorinated derivative **4-Pf** displays relatively higher thermal stability (up to 400 °C; Figure S10, SI) and proved to be also more stable in solution. The B-N fused products were fully characterized by multinuclear NMR and high-resolution MALDI-TOF mass spectrometry. ^{11}B NMR data in $CDCl_3$ revealed signals at 1.7 ppm (**4-Et**) and -2.6 ppm (**4-Pf**) as expected for a tetracoordinate configuration of the boron centers. The ^{11}B NMR signal of **4-Pf** is slightly shifted upfield compared with that of **4-Et**, consistent with the anticipated stronger B←N interaction for the more electron-deficient fluorinated derivative.

Scheme 1. Synthesis of B-N fused dianthracenylpyrazines 4 and X-ray structure plot of 4-Pf (50% thermal ellipsoids; H atoms and octane solvate omitted).

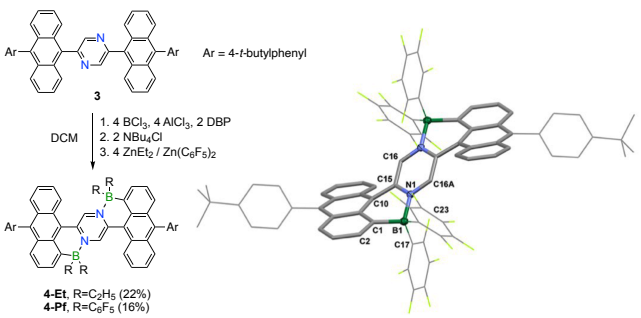

Single crystals of **4-Pf** were grown by slow evaporation of a solution in a mixture of acetone and *n*-octane. The X-ray crystal structure reveals a highly distorted, *z*-shaped conjugated framework with a large interplanar angle between the anthracene central benzene rings and the pyrazine core unit of 39.6°. In addition, the anthracene moieties themselves are buckled with an interplanar angle between the outer benzene rings of 13.0°. The B-N distances of 1.617(3) Å are on the shorter side relative to those previously found for B-N fused dipyridylanthracenes (1.628–1.685 Å).[10] This might indicate a stronger B-N interaction because the electron-withdrawing C_6F_5 groups enhance the electron-deficient character of the Lewis acidic borane moieties. The C-C bond distances between the anthracenes and the pyrazine core are also relatively short (C10-C15 1.452(3) Å), suggesting significant electronic coupling. The most severe distortion is seen in the bending of the anthracene-attached pyrazine carbon C15 out of the anthracene plane by 17.9° ($Cent_{An,inner}$-C10-C15 162.1°), a value that is larger than for any of the previously reported B-N fused pyridylanthracenes. The dislocation of the boron atom in the opposite direction relative to the anthracene moieties is less pronounced ($Cent_{An}$-C1-B1 170.2°), but still significant. The extended structure reveals square channels along the crystallographic *z*-axis that are filled with *n*-octane solvent molecules (Figure S1, SI).

To further examine the geometric features and elements of distortion for these compounds, we performed DFT calculations at the B3LYP/6-31G(d) level of theory.[14] Geometry optimizations uncovered two distinct conformational isomers for **4-Et**/**4-Pf**, one in which the core units adopt a curved saddle-like shape (*x-isomer*) and another that shows a zig-zag conformation (*z-isomer*) as found in the X-ray crystal structure of **4-Pf** (Figure 2). Contrasting the results from the X-ray analysis, in the gas phase the saddle-shaped *x-isomer* of **4-Pf** is predicted to be favored over the *z-isomer* by ΔE = 4.6 kJ mol^{-1}, whereas for **4-Et** the *x-isomer* is predicted to be more favorable by ΔE = 5.5 kJ mol^{-1} (Table S1, SI). Despite the differences in the orientation of the pyrazine relative to the central anthracene ring (more twisted for the *z-isomers*), the bond angles and distances for the conformers are overall remarkably similar and in good agreement with those of **4-Pf-z** from the X-ray analysis (Table 1). The computed geometries of compounds **4-Et**/**4-Pf** are also compared to those of the corresponding all-carbon analogs **4-Et-C** and **4-Pf-C** in Figure S2 and Table S2 (SI). Very similar geometric features are found for both the B-N Lewis pair and the all-carbon systems, suggesting that primarily steric rather than electronic effects determine the geometry.

Table 1. Computed geometric parameters (distances in Å, angles in °) for B-N fused dianthracenylpyrazines 4 (DFT, Gaussian 09; RB3LYP/6-31G(d)) and comparison to the solid-state structure of 4-Pf from X-ray diffraction.

	B-N	B-C_{An}	C_{An}-C_{Py}	C_{An}-B-N	$Cent_{An}$-C-B [b]	$Cent_{An}$-C-C_{Py} [b]	$Ph_{An,inner}$ // $Ph_{An,inner}$ [c]	$Ph_{An,inner}$ [c]// Py
4-Et-x [a]	1.639	1.619	1.462	104.8	170.6	167.2	70.7	33.0
	1.652	1.624	1.463	102.2	170.3	164.8		37.8
4-Et-z [a]	1.641	1.610	1.461	104.7	171.1	167.5	11.0	32.7
	1.651	1.626	1.463	100.9	170.4	163.9		40.3
4-Pf-x [a]	1.627	1.621	1.457	104.6	171.8	165.2	75.3	36.5
	1.653	1.615	1.456	104.5	170.0	165.1		38.9
4-Pf-z [a]	1.629	1.625	1.454	103.4	169.3	164.7 164.8	0.0	39.4
4-Pf (z) [a] X-ray	1.617(3)	1.621(3)	1.452(3)	104.7(2)	170.2	162.1	0.0	39.6

[a] Saddle-like conformers indicated with (x) and zig-zag conformers with (z). [b] $Cent_{An}$ denotes centroid of attached benzene ring. [c] $Ph_{An,inner}$ denotes central benzene ring of anthracene.

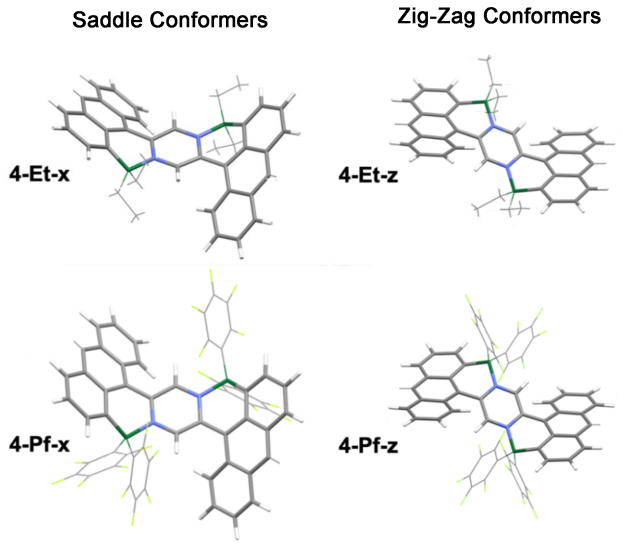

Figure 2. Computed structures of **4-Et** and **4-Pf** (Gaussian 09; RB3LYP/6-31G(d)) illustrating saddle-like conformers (x) and zig-zag conformers (z). C grey, B green, N blue, F yellow; *tert*-butylphenyl groups omitted for clarity.

Variable temperature (VT) NMR spectra acquired for **4-Pf** are consistent with rapid dynamic interconversion between isomers. At room temperature, the ^{19}F NMR spectrum of **4-Pf** showed strongly broadened peaks that split into four signals for the *ortho*- and *meta*-fluorine atoms and two signals for the *para*-fluorine atoms of the C_6F_5 rings when cooling the solution in d^8-toluene to -30 ºC (Figure S3, SI). Coalescence into one set of signals was observed with increasing temperature, which is attributed to two simultaneous processes, the hindered rotation of the individual C_6F_5 rings and the positional exchange of the C_6F_5 rings. Presumably, this exchange occurs through B-N bond dissociation followed by rotation of the $B(C_6F_5)_2$ group about the B-C(anthracene) bond.[10] The associated free energy barrier was calculated to be 53(1) kJ mol^{-1} based on the coalescence of the *p*-fluorine signals (Table S3, SI). This value is significantly lower than those previously determined for boron-fused 9,10-dipyridyl-anthracenes **A** (60–68 kJ mol^{-1}) or the mono-borylated anthracene with a sterically more hindered 2-methylpyridyl substituent (64 kJ mol^{-1}). An additional set of signals for a second isomer was not detected in the low temperature NMR spectra, suggesting that one conformational isomer is energetically strongly favored in solution.

Optoelectronic properties of B-N fused dianthracenylpyrazines. The UV-vis-NIR absorption spectra of compounds **4** were acquired in DCM solution and are illustrated in Figure 3. Compared to the precursor **3**, the absorption spectra are dramatically red-shifted, approaching the NIR region. The largest shift was observed for **4-Pf**, which shows a broad absorption band with a maximum at λ_{abs} = 774 nm and relatively little absorption throughout the visible region (400-700 nm). These results are indicative of a very narrow optical gap of E_g^{opt} = 1.67 and 1.49 eV respectively for **4-Et** and **4-Pf**. Importantly, in comparison to the B-N fused dipyridylanthracenes **C** (λ_{abs} ~535 to 555 nm, E_g^{opt} ~2.3 eV),[10] the absorptions are largely red-shifted and the gap is significantly reduced. The absorption maximum of **4-Pf** is also further shifted than that of a related B-N doped dihydroindeno[1,2-b]fluorene with partially fluorinated aryl substituents (λ_{abs} = 670 nm).[11e] The observed intense NIR absorptions were well reproduced by TD-DFT calculations performed at the PBE0/6-311+G* level of theory on the geometry-optimized structures (Table 2). According to these calculations the longest wavelength absorption is assigned to a HOMO→LUMO transition and exhibits a large oscillator strength for both isomers of **4-Et** (ϕ = 0.545 (*x*-isomer), 0.561 (z-isomer)) and **4-Pf** (ϕ = 0.559 (*x*-isomer), 0.602 (*z*-isomer)). The HOMOs for compounds **4** are mainly localized on the anthracene groups and the LUMOs on the pyrazine linker (Figure 4). The spatial separation of the HOMO and LUMO illustrates the pronounced D-A-D character of this class of molecules. Thus, significant negative solvatochromic shifts were found for compounds **4** when varying the polarity of the solvent. The absorption maxima change from λ_{max} = 698 nm (**4-Et**) and 777 nm (**4-Pf**) in toluene to λ_{max} = 648 nm (**4-Et**) and 733 nm (**4-Pf**) in acetonitrile (Figure S4 and Table S5, SI), indicative of a more polar ground state that is better stabilized by polar solvents in comparison to the first excited state. Further, while **4-Et** displayed

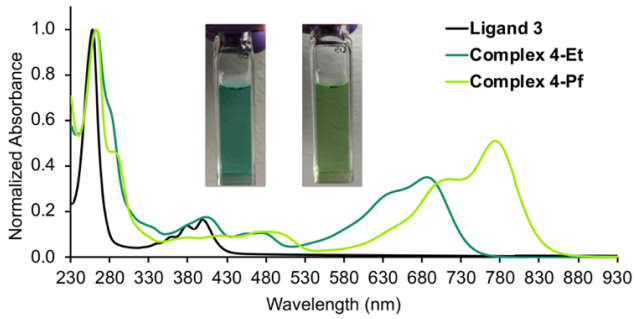

Figure 3. UV-vis absorption spectra of **3** and **4** in DCM.

Table 2. Experimental absorption data and results from DFT and TD-DFT calculations.

	Experimental			DFT/TD-DFT		
	λ_{abs} [a] (nm)	ε (10^4 $M^{-1}cm^{-1}$)	E_g^{opt} [b] (eV)	λ_{abs} [c] (nm)	T_1 [d] (eV)	S_1 [e] (eV)
4-Et	687,	3.39,	1.67	692 (*z*)	1.035 (*z*)	1.793 (*z*)
	637 (sh)	2.64		692 (*x*)	1.042 (*x*)	1.791 (*x*)
4-Pf	774,	4.00,[f]	1.49	734 (*z*)	0.970 (*z*)	1.689 (*z*)
	708 (sh)	2.76		749 (*x*)	0.948 (*x*)	1.656 (*x*)

[a] Absorption maxima in DCM solution. [b] From experimental absorption onsets. [c] Computed $S_0 \rightarrow S_1$ transition at PBE0/6-311+G(d) level. [d] Computed at UB3LYP/6-31G(d) level. [e] From TD-DFT results at S_0 geometry. [f] 1.89×10^4 $M^{-1}cm^{-1}$ at 808 nm.

weak fluorescence at 784 nm at 293 K that was enhanced at 77 K, **4-Pf** was essentially non-emissive in MeTHF solution at room temperature and at 77 K (Figure S5, SI). The weak fluorescence for **4-Et** and lack of fluorescence for **4-Pf** indicates that the excited state decays through nonradiative pathways. The radiative and nonradiative decay rates for weakly emissive **4-Et** were estimated from the quantum yield (Φ = 1.6%) and lifetime (τ = 0.55 ns) to be 2.9×10^7 s^{-1} and 180×10^7 s^{-1} (Table S6). The radiative decay rate is similar to that of dipyridylanthrancene-based systems that emit at shorter wavelengths of ca. 620 nm,[10] but the nonradiative decay rate is about 50 times larger. Rapid non-radiative decay of these NIR chromophores is consistent with the band gap law[15] and may be further promoted by the molecular flexibility deduced from the VT NMR studies.

To further examine the electronic structure and verify the electron acceptor properties of the B-N fused dianthracenylpyrazines, we acquired cyclic (CV) and square wave voltammograms (SWV) for **4-Et** / **4-Pf** in THF containing 0.1 M $Bu_4N[PF_6]$. **4-Pf** exhibits two consecutive reversible reduction processes at E_{red} = -0.74 and -1.75 V and **4-Et** at E_{red} = -1.23, -2.10 V relative to the $Fc^{0/+}$ couple (Figure S6 and Table S7, SI). While both compounds are readily reduced, the first reduction for **4-Pf** occurs at a far less negative potential than for **4-Et** due to the electron-withdrawing nature of the C_6F_5 substituents that further increase the electron-deficient character. Oxidative scans were performed in CH_2Cl_2 containing 0.1 M $Bu_4N[PF_6]$. **4-Pf** undergoes two reversible oxidations, whereas **4-Et** shows only irreversible processes. The HOMO and LUMO levels were estimated from the electrochemical redox potentials and are given in Table S8 (SI). Most remarkable are the very low lying LUMO orbital levels of -3.90 / -4.39 eV for **4-Et** / **4-Pf**. The HOMO-LUMO gaps are overall in good agreement with the trends from DFT results (*vide infra*) and the optical gaps deduced from UV-Vis absorption spectroscopy.

The role of the B-N Lewis pair functionalization in endowing compounds **4** with such a strong acceptor character can be assessed by comparing the frontier orbital energies with those of the all-carbon analogs using computational methods. The computed frontier orbitals for the *z-isomers* of the B-N fused

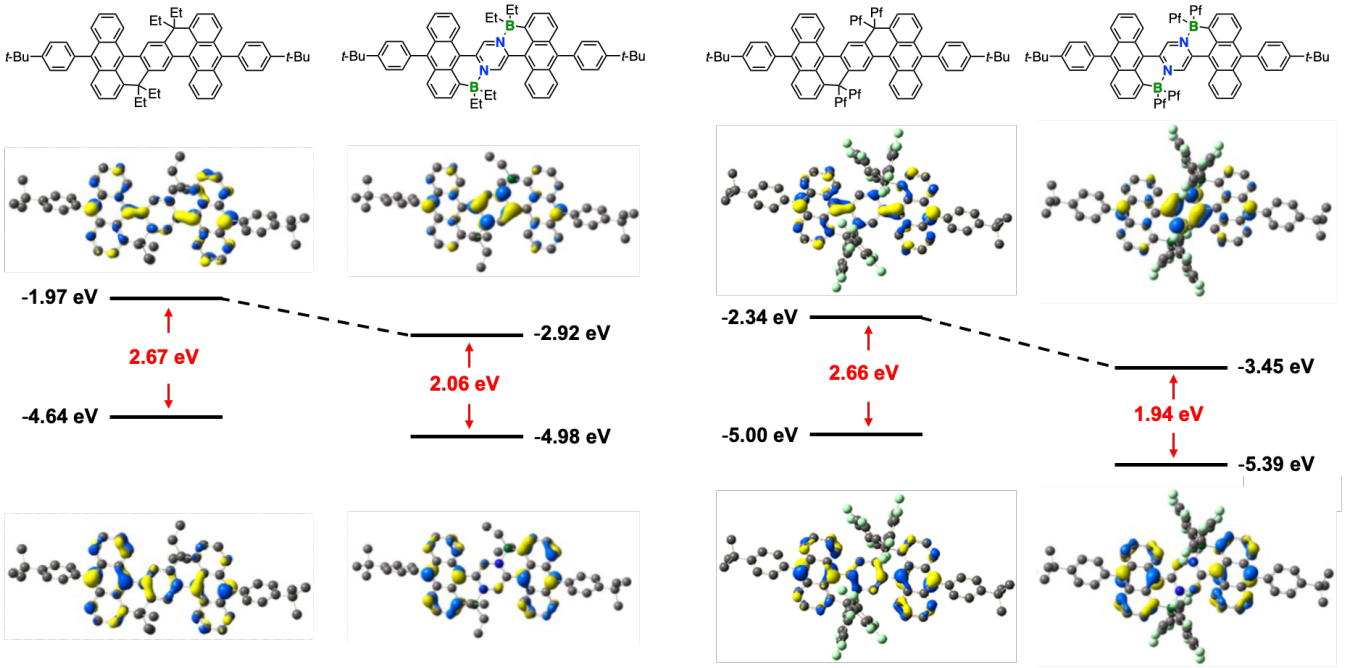

Figure 4. Computed frontier orbital energies and HOMO/LUMO orbital plots of **4-Et** / **4-Pf** (*z-isomers*) in comparison to their all-carbon analogs **4-Et-C** / **4-Pf-C** (DFT, RB3LYP/6-31G(d)).

dianthracenylpyrazines and their all-carbon analogs are illustrated in Figure 4. The corresponding results for the *x-isomers* are qualitatively similar and are provided in the SI (Figure S8, Table S9). The B-N fused dianthracenylpyrazines **4-Et** / **4-Pf** show slightly decreased HOMO and much more dramatically decreased LUMO energy levels relative to the all-carbon analogs **4-Et-C** / **4-Pf-C** (and even more so the non-fused precursor 3, see Figure S8). This leads to far smaller HOMO-LUMO energy gaps (E_g) for **4-Et** / **4-Pf** of 2.06 / 1.94 eV, respectively, effectively lowering E_g relative to the all-carbon analogs by 0.61 / 0.72 eV and relative to non-fused **3** by 1.22 / 1.34 eV. The attachment of electron-withdrawing C_6F_5 groups to boron further lowers the HOMO-LUMO gap, in good agreement with the red-shift of the longest wavelength absorption of **4-Pf** in comparison to that of **4-Et**. Closer inspection of the orbital distributions reveals major differences in the electronic structure for the B-N versus the all-carbon systems. The HOMO and LUMO orbitals for the all-carbon analogs **4-Et-C** / **4-Pf-C** show contributions from the anthracene and pyrazine groups, in sharp contrast to the spatial separation of the HOMO and LUMO in borylated **4-Et** / **4-Pf**.

In our prior studies, we found that an intriguing characteristic of B-N functionalized anthracenes is their ability to readily react with oxygen and to form singlet oxygen.[10,16] To investigate the ability of the B-N fused dianthracenylpyrazines **4-Et** / **4-Pf** to act as a singlet oxygen sensitizer, solutions of the acenes and excess 9,10-dimethylanthracene (DMA) as a singlet oxygen acceptor in air-saturated CH_2Cl_2 were irradiated with a panchromatic light source at room temperature (Figures S11-S12). Indeed, compound **4-Et** promotes conversion of DMA into its endoperoxide. However, when using the more electron-deficient compound **4-Pf** with its lower-lying HOMO/LUMO and smaller HOMO-LUMO gap as a photosensitizer, only negligible amounts of DMA were converted upon photoirradiation under otherwise identical conditions. Besides the lower lying HOMO, the relatively smaller S_0-T_1 gap of **4-Pf** (computed as 0.95/0.97 eV, Table 2) may also disfavor the conversion of triplet to singlet oxygen as it is at the borderline of the energy required for this process of 0.98 eV.[17] Both the lack of emission and low reactive oxygen species (ROS) generation of **4-Pf** further suggest that vibrational (conformational flexibility) and/or rotational (*tert*-butyl, B-ethyl) relaxation processes play a prominent role in the excited state deactivation, thereby enhancing photothermal conversion.[9f,9j] Thus, the strong absorbance of **4-Pf** in the NIR region, in stark contrast to the non-borylated precursor, was postulated to enable high efficiency photothermal conversion, suggesting opportunities for PTT application.

B-N fused dianthracenylpyrazines as photothermal agents (PTAs) and *in vitro* cell assays. To explore **4-Pf** as a bioavailable PTA, we prepared water-soluble nanoparticles via nanoprecipitation using an amphiphilic biocompatible copolymer 1,2-distearoyl-sn-glycero-3-phosphoethanol-amine-N-[methoxy-(polyethylene glycol)-2000] (DSPE-mPEG$_{2000}$) as the encapsulation matrix. Nanoparticles **4-Pf-NPs** can be homogeneously dispersed in water, yielding a green colored solution. A strong absorption band in the spectral region of 700-900 nm (Figure S13) is consistent with the absorption of **4-Pf** in DCM solution, suggesting a pronounced capability to absorb light in the NIR region (ε_{778} = 3.80×10^4 M^{-1}cm^{-1}, ε_{808} = 2.36×10^4 M^{-1}cm^{-1}). The morphology of **4-Pf-NPs** was characterized by transmission electron microscopy (TEM), which revealed uniform spherical particles with an average diameter of 8 nm (Figure 5a). Dynamic light scattering (DLS) measurements gave similar average hydrodynamic diameters of ca. 12 nm (Figure 5a) with a zeta potential of -7.8 mV. The **4-Pf-NPs** solution was clear and the absorption spectrum did not display any significant variation after storage at 4 °C for 21 days (Figure S13, SI), suggesting good physiological stability in aqueous solutions. Next, the photothermal effect of **4-Pf-NPs** in water was investigated under NIR laser irradiation at 808 nm with a power density of 1.0 W cm^{-2}. As shown in Figure 5b-c, the temperature of **4-Pf-NPs** solutions at different concentrations gradually increased under irradiation and a high value of 62.8 °C was recorded within 600 s at a 50 μM concentration, whereas pure water did not show any significant temperature change. Meanwhile, **4-Pf-NPs** showed an obvious laser-power-density-dependent temperature elevation property (Figure S17-18, SI). The PCE value of **4-Pf-NPs** at 808 nm was calculated as 41.8 % (Figure S14-S15, SI), which is comparable to that of various state-of-the-art small molecule photothermal agents (Table S13 and Figure S21, SI), highlighting the potential of **4-Pf-NPs** as a PTT agent.

Encouraged by the good PTT performance of **4-Pf-NPs** in water, the biocompatibility and photocytotoxicity was further evaluated by performing a CCK-8 assay. Without laser irradiation, 4T1 cells incubated with **4-Pf-NPs** maintained a high cell viability of more than 95% even at concentrations as high as 35 μM, demonstrating good biocompatibility of **4-Pf-NPs** (Figure 5d). In contrast, upon irradiation with a 1.0 W cm^{-2} (808 nm) laser for 5 min, the cell viabilities distinctly decreased with increasing concentration of **4-Pf-NPs**, within a half maximal inhibitory concentration (IC_{50}) of 13.7 μM (Figure 5d). Next, a Calcein AM and propidium iodide (PI) assay was employed to evaluate the apoptosis and necrosis rates that distinguish viable cells (in green color) from dead cells (in red color). It can be seen in Figure 5e that the cells with **4-Pf-NPs** when exposed to NIR irradiation showed obvious red fluorescence and negligible green fluorescence indicating substantial cell death. In contrast, cells in the presence of **4-Pf-NPs** without light, cells exposed to NIR irradiation without **4-Pf-NPs**, and a control group all exhibited strong green fluorescence and no red fluorescence, demonstrating the absence of any toxic effects on the cells. We further investigated the possible death mechanism of **4-Pf-NPs**-induced cytotoxicity by flow cytometry with Annexin V-FITC and propidium iodide (PI) (Figure 5f). After incubation with **4-Pf-NPs** and NIR irradiation, the percentage of viable cells decreased from 90.0% (PBS) to 14.4%, and more than 84% of the cells were in the apoptosis stage or necrosis stage. In contrast, neither **4-Pf-NPs** nor NIR irradiation alone inhibited cell growth. These results further confirmed the efficient photothermal effect of **4-Pf-NPs** on cells under laser irradiation, suggesting great potential for *in vivo* cancer cell ablation.

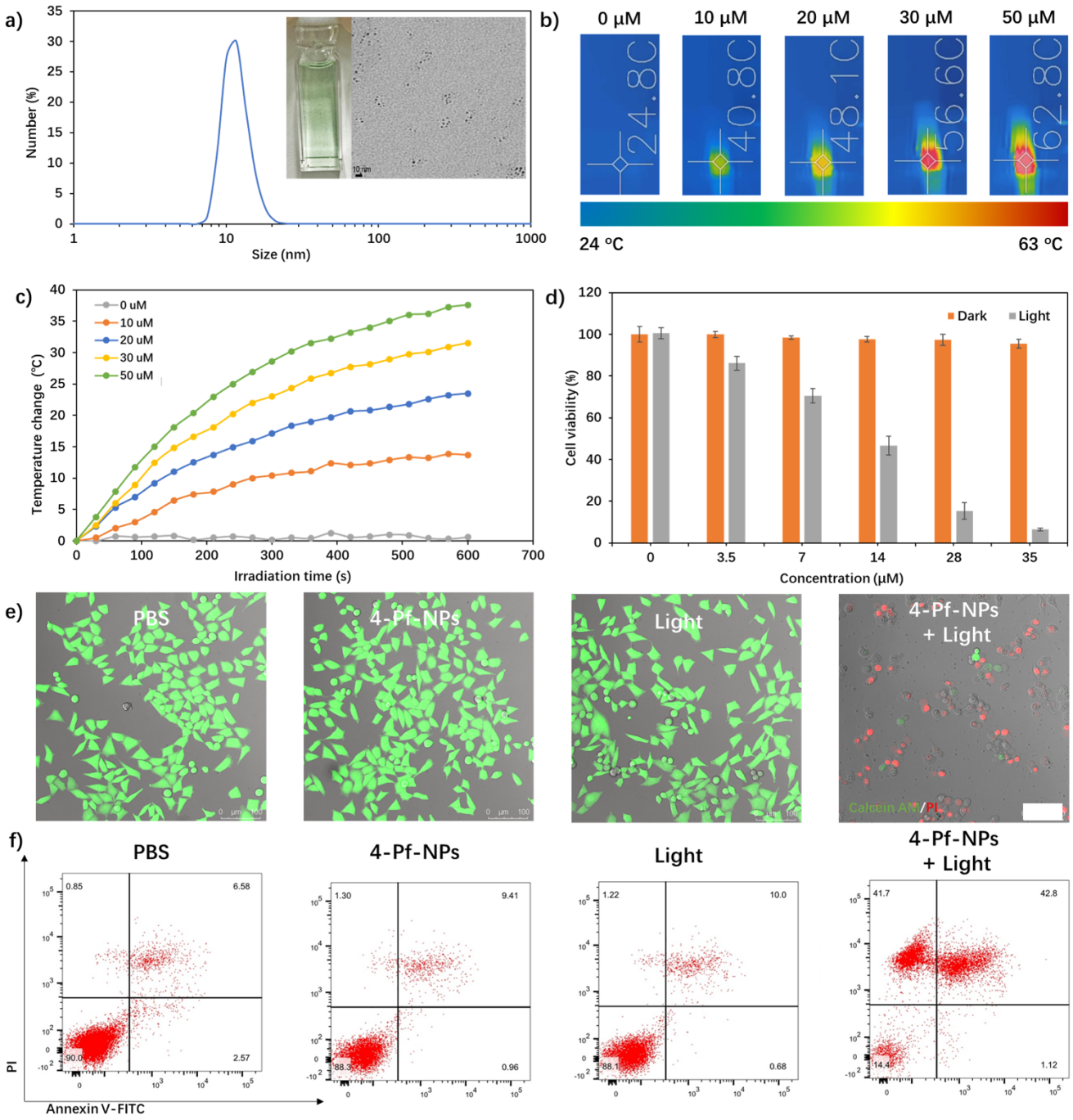

Figure 5. a) The size distribution of **4-Pf-NPs** measured using dynamic light scattering (DLS) in water. Insets: photographs of **4-Pf-NPs** dispersed in water and TEM images of **4-Pf-NPs** (scale bar: 10 nm); b) Thermal images of **4-Pf-NPs** at different concentrations (0-50 μM) after 808 nm light irradiation; c) Photothermal conversion behavior of **4-Pf-NPs** at different concentrations (0-50 μM) under 808 nm light irradiation; d) Cell viability of 4T1 cells incubated with **4-Pf-NPs** at various concentrations in the dark and after NIR light irradiation (808 nm, 1.0 W cm^{-2}, 5 min) (n = 3, Mean ± S.D.); e) Calcein AM (green) and propidium iodide (red) merged fluorescence imaging of 4T1 cells after different treatments. NIR light irradiation (808 nm, 1.0 W cm^{-2}, 5 min) was conducted after cells were incubated with **4-Pf-NPs** (28 μM). Scale bar: 100 μm; f) Apoptosis and necrosis analysis using flow cytometry toward 4T1 cells after different treatments. NIR light irradiation (808 nm, 1.0 W cm^{-2}, 5 min) was conducted after cells were incubated with **4-Pf-NPs** (28 μM).

***In vivo* tumor treatment studies.** To investigate the PTT effect *in vivo*, four groups (four mice for each group) were randomly established using 4T1 tumor-bearing mice, as follows: "Control" (PBS), "Light" (PBS with laser irradiation), "**4-Pf-NPs**", and "**4-Pf-NPs** + Light". After intravenous injection of PBS and **4-Pf-NPs** (100 μL, 700 μM) for 24 h, the mice from the groups with laser were irradiated (808 nm, 1.0 W cm^{-2}) for 5 min, and the tumor temperatures were monitored by an infrared thermal camera. The mice of the "**4-Pf-NPs** + Light" group displayed a rapid temperature increase to 49.7 °C within 1 min irradiation and the temperature slowly rose to 54 °C for the remaining time (Figure 6a-b), which was high enough to destroy the tumor cells.

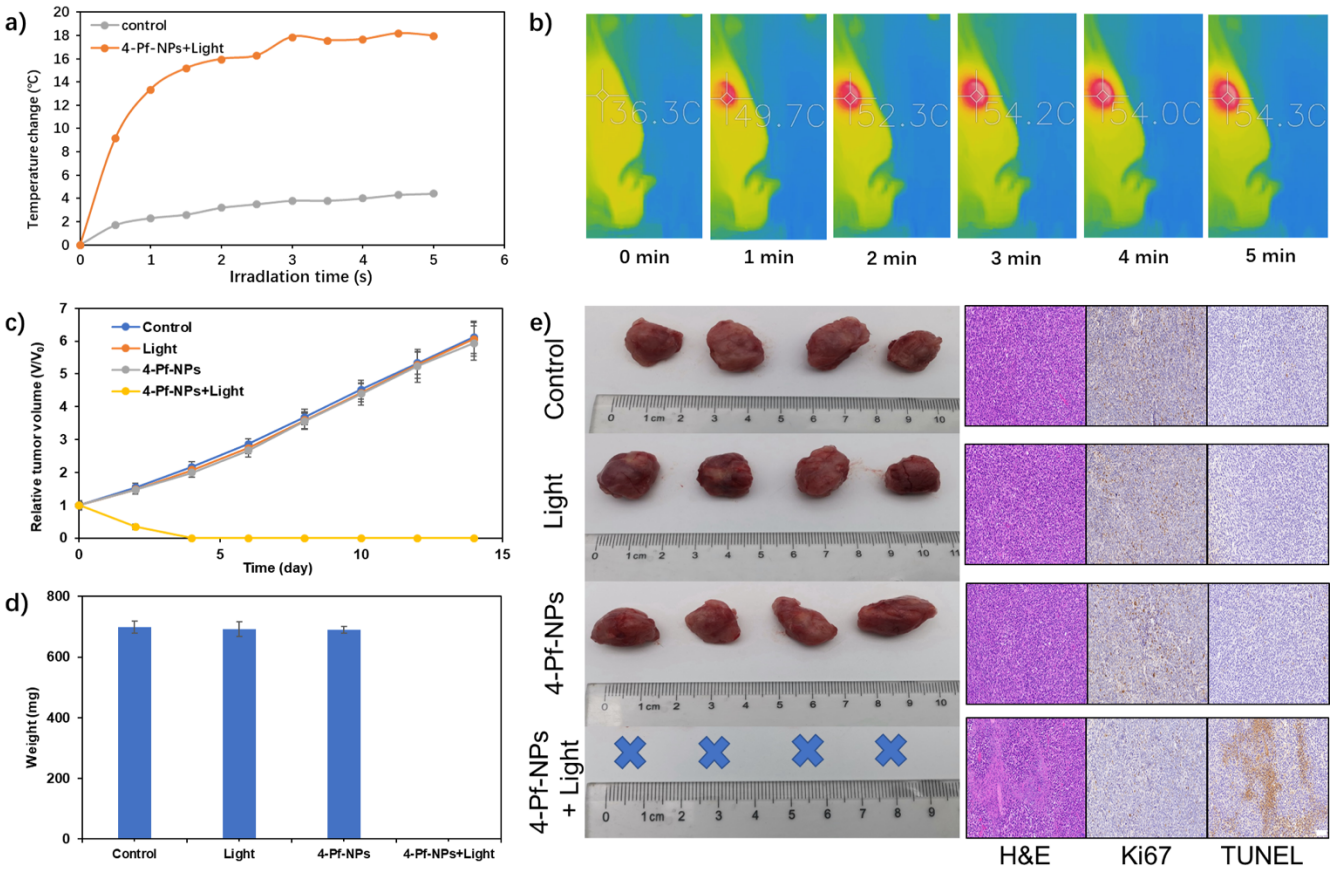

Figure 6. a) Temperature change curves of 4T1 tumors in mice treated with or without **4-Pf-NPs** and laser irradiation as a function of irradiation time; b) Thermal IR images of 4T1 tumor-bearing mice after intravenous injection of **4-Pf-NPs** and exposure to 1.0 W cm^{-2} (808 nm) laser irradiation for 5 min; c) The relative tumor volume (V/V_0) of each group during treatments (n = 5, Mean ± S.D.); d) Average weights of tumors at day 14 after treatment (n = 5, Mean ± S.D.); e) Representative photos of the excised tumors at day 14 after treatment and Histological H&E, Ki67 staining, and fluorescence TUNEL of tumor tissues collected from mice in the different groups at day 2, 24 h after laser treatment. The scale bar is 100 μm.

In contrast, the control group ("PBS + Light") exhibited negligible temperature variation ($\Delta T \approx 4$ °C) under the same irradiation condition, indicating strong photothermal conversion ability of **4-Pf-NPs** *in vivo*. Following above treatments, the PTT efficiency of each group was evaluated by monitoring the tumor growth for 14 days. As depicted in Figure 6c, the treatments of "PBS + Light" and "**4-Pf-NPs**" failed to inhibit the tumor growth (average tumor volume increased 6-fold), similar to the "Control" group, indicating that only laser irradiation or the presence of **4-Pf-NPs** themselves had a negligible benefit in cancer therapy. Remarkably, the "**4-Pf-NPs** + Light" group exhibited high antitumor efficacy, where the tumor was totally eradicated without recurrence. The above results were further confirmed by the tumor weight and photographs after different treatments (Figure 6d-e). One mouse from each group was sacrificed on day 2 (24 h later of laser treatment) and the tumor tissues were collected for pathological examination by hematoxylin & eosin (H&E), TdT-mediated dUTP Nick-End Labeling (TUNEL) and Antigen Ki-67 staining. H&E staining clearly revealed much more necrotic areas in the "**4-Pf-NPs** + Light" group. Moreover, both TUNEL and Antigen Ki-67 staining demonstrated that "**4-Pf-NPs** + Light" is the most effective treatment in inducing apoptosis and inhibiting tumor cell proliferation (Figure 6e). In addition, no notable abnormalities and lesions were observed in the tissue sections of the heart, liver, spleen, lung, and kidney in all the groups (Figure S25, SI). It is worth noting that no significant difference of the mice weight was observed for all groups (Figure S26, SI). Finally, the toxicity of **4-Pf-NPs** was also estimated in healthy mice. There were negligible influences on body weight changes of mice during two weeks feeding (Figure S27, SI). The assay of complete blood panel in the treated group showed no statistical differences with those in the control group (Figure S28-29, SI). No noticeable pathological change or tissue denaturation was found in all main organs (Figure S30, SI). All these results clearly confirmed the remarkable therapeutic effect of **4-Pf-NPs** with excellent biocompatibility and minor side effects for cancer therapy.

CONCLUSION

We have designed and synthesized two new B-N fused dianthracenylpyrazine derivatives with exceptionally narrow HOMO-LUMO gaps. An X-ray crystal structure of the C_6F_5-substituted derivative **4-Pf** reveals a *z*-shaped conformation in the solid state with large angles between the anthracenyl

groups and the central pyrazine moiety. An alternative conformer with a saddle-shape was identified by computational methods, which predict this isomer to be slightly more favorable by ca. 5 kJ mol^{-1} in the gas phase. Incorporation of the B-N units into the conjugated systems leads to major changes in the electronic structure compared to their C-C analogs, including dramatically lower LUMO levels and large decreases in the HOMO-LUMO gap. Thus, the borylated dianthracenylpyrazine derivatives show significant absorbance at greater than 700 nm. DFT calculations reveal the D-A-D character of these B-N fused dianthracenylpyrazines as seen in the spatial separation of the HOMO and LUMO orbitals and confirm the strong overall acceptor character. Benefiting from intramolecular charge transfer, absence of fluorescence, as well as good photostability, the nanostructured **4-Pf-NPs** show excellent photothermal conversion efficiency of 41.8%. Both *in vitro* and *in vivo* experiments validate the promising biocompatibility and excellent photothermal therapeutic efficacy of **4-Pf-NPs**. These results indicate that the B-N Lewis pair functionalization of PAHs is a promising new strategy toward NIR absorbing materials that serve as effective PTAs. Thus, this study is expected to trigger further advances in the molecular engineering of NIR absorbing dyes based on B-N fused PAHs for biomedical applications.

ASSOCIATED CONTENT

Supporting Information

The Supporting Information is available free of charge on the ACS Publications website.

Experimental Details and Characterization Data (PDF)

Movie Illustrating Photothermal Effect (mp4)

X-ray Crystallographic Data (CIF)

AUTHOR INFORMATION

Corresponding Author

* Frieder Jäkle, fjaekle@rutgers.edu; Kanglei Liu, kanglei_liu@bit.edu.cn; Zhenqi Jiang, 7520200073@bit.edu.cn

Author Contributions

The manuscript was written through contributions of all authors. All authors have given approval to the final version of the manuscript.

Funding Sources

Any funds used to support the research of the manuscript should be placed here (per journal style).

Notes

The authors declare no conflict of interest.

ACKNOWLEDGMENT

This material is based upon work supported by the US National Science Foundation (NSF) under Grants CHE-1664975 and CHE-1954122. K. L. thanks the National Natural Science Foundation of China (Grant 22101025) for support. Z. J. thanks the National Natural Science Foundation of China (Grant 32101153) for support. A 500 MHz NMR spectrometer (MRI 1229030) and an X-ray diffractometer (CRIF 0443538) used in these studies were purchased with support from the NSF and Rutgers University. We thank Dr. Lazaros Kakalis for acquisition of 2D NMR data.

REFERENCES

1. (a) Anthony, J. E., Functionalized acenes and heteroacenes for organic electronics. *Chem. Rev.* **2006**, *106*, 5028-5048. (b) Shirota, Y.; Kageyama, H., Charge carrier transporting molecular materials and their applications in devices. *Chem. Rev.* **2007**, *107*, 953-1010. (c) Anthony, J. E.; Facchetti, A.; Heeney, M.; Marder, S. R.; Zhan, X. W., n-Type Organic Semiconductors in Organic Electronics. *Adv. Mater.* **2010**, *22*, 3876-3892. (d) Ding, D.; Li, K.; Liu, B.; Tang, B. Z., Bioprobes Based on AIE Fluorogens. *Acc. Chem. Res.* **2013**, *46*, 2441-2453. (e) Narita, A.; Wang, X. Y.; Feng, X. L.; Müllen, K., New advances in nanographene chemistry. *Chem. Soc. Rev.* **2015**, *44*, 6616-6643. (f) Zhang, G. Y.; Zhao, J. B.; Chow, P. C. Y.; Jiang, K.; Zhang, J. Q.; Zhu, Z. L.; Zhang, J.; Huang, F.; Yan, H., Nonfullerene Acceptor Molecules for Bulk Heterojunction Organic Solar Cells. *Chem. Rev.* **2018**, *118*, 3447-3507.

2. (a) Qian, G.; Wang, Z. Y., Near-Infrared Organic Compounds and Emerging Applications. *Chem.-Asian J.* **2010**, *5*, 1006-1029. (b) Guo, Z. Q.; Park, S.; Yoon, J.; Shin, I., Recent progress in the development of near-infrared fluorescent probes for bioimaging applications. *Chem. Soc. Rev.* **2014**, *43*, 16-29. (c) Hong, G.; Antaris, A. L.; Dai, H., Near-infrared fluorophores for biomedical imaging. *Nat. Biomed. Eng.* **2017**, *1*, 0010. (d) Li, J.-B.; Liu, H.-W.; Fu, T.; Wang, R.; Zhang, X.-B.; Tan, W., Recent Progress in Small-Molecule Near-IR Probes for Bioimaging. *Trends Chem.* **2019**, *1*, 224-234. (e) Wang, K.; Lv, J.; Duan, T.; Li, Z.; Yang, Q.; Fu, J.; Meng, W.; Xu, T.; Xiao, Z.; Kan, Z.; Sun, K.; Lu, S., Simple near-Infrared Nonfullerene Acceptors Enable Organic Solar Cells with >9% Efficiency. *ACS Appl. Mater. Inter.* **2019**, *11*, 6717-6723. (f) Lee, J.; Cha, H.; Yao, H. F.; Hou, J. H.; Suh, Y. H.; Jeong, S.; Lee, K.; Durrant, J. R., Toward Visibly Transparent Organic Photovoltaic Cells Based on a Near-Infrared Harvesting Bulk Heterojunction Blend. *ACS Appl. Mater. Inter.* **2020**, *12*, 32764-32770.

3. (a) Cheng, L.; Wang, C.; Feng, L. Z.; Yang, K.; Liu, Z., Functional Nanomaterials for Phototherapies of Cancer. *Chem. Rev.* **2014**, *114*, 10869-10939. (b) Liu, Y. J.; Bhattarai, P.; Dai, Z. F.; Chen, X. Y., Photothermal therapy and photoacoustic imaging via nanotheranostics in fighting cancer. *Chem. Soc. Rev.* **2019**, *48*, 2053-2108. (c) Feng, G. X.; Zhang, G. Q.; Ding, D., Design of superior phototheranostic agents guided by Jablonski diagrams. *Chem. Soc. Rev.* **2020**, *49*, 8179-8234. (d) Cao, Y. Y.; Dou, J. H.; Zhao, N. J.; Zhang, S. M.; Zheng, Y. Q.; Zhang, J. P.; Wang, J. Y.; Pei, J.; Wang, Y. P., Highly Efficient NIR-II Photothermal Conversion Based on an Organic Conjugated Polymer. *Chem. Mater.* **2017**, *29*, 718-725. (e) Xu, X.-Q.; Liao, H.; Liu, H.; Chu, Y.; He, Y.; Wang, Y., A Water-Soluble Photothermal Host–Guest Complex with pH-Sensitive Super-large Redshift Absorption. *CCS Chem.* **2020**, *3*, 2520-2259. (f) Chu, Y.; Liao, S.; Liao, H.; Lu, Y.; Geng, X.; Wu, D.; Pei, J.; Wang, Y., Second Near-Infrared Photothermal Therapy with Superior Penetrability through Skin Tissues. *CCS Chem.* **2021**, *3*, 3289-3300.

4. (a) Yamaguchi, S.; Tamao, K., A key role of orbital interaction in the main group element-containing p-electron systems. *Chem. Lett.* **2005**, *34*, 2-7. (b) Escande, A.; Ingleson, M. J., Fused polycyclic aromatics incorporating boron in the core: fundamentals and applications. *Chem. Commun.* **2015**, *51*, 6257-6274. (c) Ji, L.; Griesbeck, S.; Marder, T. B., Recent developments in and perspectives on three-coordinate boron materials: a bright future. *Chem. Sci.* **2017**, *8*, 846-863. (d) Stępień, M.; Gońka, E.; Żyła, M.; Sprutta, N., Heterocyclic Nanographenes and Other Polycyclic Heteroaromatic Compounds: Synthetic Routes, Properties, and Applications. *Chem. Rev.* **2017**, *117*, 3479–3716. (e) Szűcs, R.; Bouit, P.-A.; Nyulászi, L.; Hissler, M., Phosphorus-Containing Polycyclic Aromatic Hydrocarbons. *ChemPhysChem* **2017**, *18*, 2618-2630. (f) von Grotthuss, E.; John, A.; Kaese, T.; Wagner, M., Doping Polycyclic Aromatics with Boron for Superior Performance in Materials Science and Catalysis. *Asian J. Org. Chem.* **2018**, *7*, 37-53. (g) Baumgartner, T.; Jäkle, F., *Main group strategies towards functional hybrid materials*. John Wiley & Sons: Hoboken, NJ, 2018.

(h) Mellerup, S. K.; Wang, S., Boron-Doped Molecules for Optoelectronics. *Trends Chem.* **2019**, *1*, 77-89. (i) Berger, S. M.; Marder, T. B., Applications of triarylborane materials in cell imaging and sensing of bio-relevant molecules such as DNA, RNA, and proteins. *Mater. Horiz.* **2022**, *9*, 112-120.

5. (a) Wakamiya A., Taniguchi T., Yamaguchi S., Intramolecular B-N Coordination as a Scaffold for Electron-Transporting Materials: Synthesis and Properties of Boryl-Substituted Thienylthiazoles. *Angew. Chem. Int. Ed.* **2006**, *45*, 3170-3173. (b) Liu, Z. Q.; Marder, T. B., B-N versus C-C: How similar are they? *Angew. Chem. Int. Ed.* **2008**, *47*, 242-244. (c) Li, D.; Zhang, H. Y.; Wang, Y., Four-coordinate organoboron compounds for organic light-emitting diodes (OLEDs). *Chem. Soc. Rev.* **2013**, *42*, 8416-8433. (d) Huang, J. H.; Li, Y. Q., BN Embedded Polycyclic pi-Conjugated Systems: Synthesis, Optoelectronic Properties, and Photovoltaic Applications. *Front. Chem.* **2018**, *6*, 341. (e) Haque, A.; Al-Balushi, R. A.; Raithby, P. R.; Khan, M. S., Recent Advances in pi-Conjugated NC-Chelate Organoboron Materials. *Molecules* **2020**, *25*, 2645.

6. (a) Yusuf, M.; Liu, K. L.; Guo, F.; Lalancette, R. A.; Jäkle, F., Luminescent organoboron ladder compounds via directed electrophilic aromatic C-H borylation. *Dalton Trans.* **2016**, *45*, 4580-4587. (b) Bachollet, S. P. J. T.; Volz, D.; Fiser, B.; Munch, S.; Ronicke, F.; Carrillo, J.; Adams, H.; Schepers, U.; Gomez-Bengoa, E.; Brase, S.; Harrity, J. P. A., A Modular Class of Fluorescent Difluoroboranes: Synthesis, Structure, Optical Properties, Theoretical Calculations and Applications for Biological Imaging. *Chem. Eur. J.* **2016**, *22*, 12430-12438. (c) Zhao, R. Y.; Dou, C. D.; Xie, Z. Y.; Liu, J.; Wang, L. X., Polymer Acceptor Based on BN Units with Enhanced Electron Mobility for Efficient All-Polymer Solar Cells. *Angew. Chem. Int. Ed.* **2016**, *55*, 5313-5317. (d) Shen, C. S.; Srebro-Hooper, M.; Jean, M.; Vanthuyne, N.; Toupet, L.; Williams, J. A. G.; Torres, A. R.; Riives, A. J.; Muller, G.; Autschbach, J.; Crassous, J., Synthesis and Chiroptical Properties of Hexa-, Octa-, and Deca-azaborahelicenes: Influence of Helicene Size and of the Number of Boron Atoms. *Chem.-Eur. J.* **2017**, *23*, 407-418. (e) Alahmadi, A. F.; Lalancette, R. A.; Jäkle, F., Highly Luminescent Ladderized Fluorene Copolymers Based on B-N Lewis Pair Functionalization. *Macromol. Rapid Comm.* **2018**, *39*, 1800456. (f) Dominguez, Z.; Lopez-Rodriguez, R.; Alvarez, E.; Abbate, S.; Longhi, G.; Pischel, U.; Ros, A., Azabora[5]helicene Charge-Transfer Dyes Show Efficient and Spectrally Variable Circularly Polarized Luminescence. *Chem.-Eur. J.* **2018**, *24*, 12660-12668. (g) Grandl, M.; Schepper, J.; Maity, S.; Peukert, A.; von Hauff, E.; Pammer, F., N -> B Ladder Polymers Prepared by Postfunctionalization: Tuning of Electron Affinity and Evaluation as Acceptors in All-Polymer Solar Cells. *Macromolecules* **2019**, *52*, 1013-1024. (h) Vanga, M.; Lalancette, R. A.; Jäkle, F., Controlling the Optoelectronic Properties of Pyrene by Regioselective Lewis Base-Directed Electrophilic Aromatic Borylation. *Chem. Eur. J.* **2019**, *25*, 10133-10140. (i) Vanga, M.; Sa, S.; Kumari, A.; Murali, A. C.; Nayak, P.; Das, R.; Venkatasubbaiah, K., Synthesis of pi-extended B <- N coordinated phenanthroimidazole dimers and their linear and nonlinear optical properties. *Dalton Trans.* **2020**, *49*, 7737-7746. (j) Zhang, P. F.; Zeng, J. C.; Zhuang, F. D.; Zhao, K. X.; Sun, Z. H.; Yao, Z. F.; Lu, Y.; Wang, X. Y.; Wang, J. Y.; Pei, J., Parent B2N2-Perylenes with Different BN Orientations. *Angew. Chem. Int. Ed.* **2021**, *60*, 23313-23319. (k) Sakamaki, T.; Nakamuro, T.; Yamashita, K.; Hirata, K.; Shang, R.; Nakamura, E., B2N2-Doped Dibenzo[a,m]Rubicene: Modular Synthesis, Properties, and Coordination-Induced Color Tunability. *Chem. Mater.* **2021**, *33*, 5337-5344. (l) Full, J.; Panchal, S. P.; Götz, J.; Krause, A.-M.; Nowak-Król, A., Modular Synthesis of Organoboron Helically Chiral Compounds: Cutouts from Extended Helices. *Angew. Chem. Int. Ed.* **2021**, *60*, 4350-4357. (m) Vanga, M.; Sahoo, A.; Lalancette, R. A.; Jäkle, F., Linear Extension of Anthracene via B <- N Lewis Pair Formation: Effects on Optoelectronic Properties and Singlet O_2 Sensitization. *Angew. Chem. Int. Ed.* **2022**, *61*, e202113075. (n) Meng, G. Y.; Liu, L. J.; He, Z. C.; Hall, D.; Wang, X.; Peng, T.; Yin, X. D.; Chen, P. K.; Beljonne, D.; Olivier, Y.; Zysman-Colman, E.; Wang, N.; Wang, S. N., Multi-resonant thermally activated delayed fluorescence emitters based on tetracoordinate boron-containing PAHs: colour tuning based on the nature of chelates. *Chem. Sci.* **2022**, *13*, 1665-1674. (o) Feng, Y.; Zhou, J.; Qiu, H.; Schnitzlein, M.; Hu, J.; Liu, L.; Würthner, F.; Xie, Z., Boron-Locked Starazine – A Soluble and Fluorescent Analogue of Starphene. *Chem. Eur. J.* **2022**, *28*, e202200770.

7. (a) Cao, Y.; Nagle, J. K.; Wolf, M. O.; Patrick, B. O., Tunable Luminescence of Bithiophene-Based Flexible Lewis Pairs. *J. Am. Chem. Soc.* **2015**, *137*, 4888-4891. (b) Zhu, C. Z.; Fang, L., Locking the Coplanar Conformation of π-Conjugated Molecules and Macromolecules Using Dynamic Noncovalent Bonds. *Macromol. Rapid Commun.* **2018**, *39*, 1700241. (c) Mellerup, S. K.; Wang, S. N., Boron-based stimuli responsive materials. *Chem. Soc. Rev.* **2019**, *48*, 3537-3549. (d) Koch, R.; Sun, Y.; Orthaber, A.; Pierik, A. J.; Pammer, F., Turn-on fluorescence sensors based on dynamic intramolecular N -> B-coordination. *Org. Chem. Front.* **2020**, *7*, 1437-1452.

8. (a) Crossley, D. L.; Vitorica-Yrezabal, I.; Humphries, M. J.; Turner, M. L.; Ingleson, M. J., Highly Emissive Far Red/Near-IR Fluorophores Based on Borylated Fluorene-Benzothiadiazole Donor-Acceptor Materials. *Chem. Eur. J.* **2016**, *22*, 12439-12448. (b) Nakamura, T.; Furukawa, S.; Nakamura, E., Benzodipyrrole-based Donor-Acceptor-type Boron Complexes as Tunable Near-infrared-Absorbing Materials. *Chem.-Asian J.* **2016**, *11*, 2016-2020. (c) Dash, B. P.; Hamilton, I.; Tate, D. J.; Crossley, D. L.; Kim, J. S.; Ingleson, M. J.; Turner, M. L., Benzoselenadiazole and benzotriazole directed electrophilic C-H borylation of conjugated donor-acceptor materials. *J. Mater. Chem. C* **2019**, *7*, 718-724. (d) Maar, R. R.; Zhang, R. Z.; Stephens, D. G.; Ding, Z. F.; Gilroy, J. B., Near-Infrared Photoluminescence and Electrochemiluminescence from a Remarkably Simple Boron Difluoride Formazanate Dye. *Angew. Chem. Int. Ed.* **2019**, *58*, 1052-1056. (e) Min, Y.; Dou, C. D.; Tian, H. K.; Liu, J.; Wang, L. X., A disk-type polyarene containing four B <- N units. *Chem. Commun.* **2019**, *55*, 3638-3641.

9. (a) Tang, Q. Y.; Xiao, W. Y.; Huang, C. H.; Si, W. L.; Shao, J. J.; Huang, W.; Chen, P.; Zhang, Q.; Dong, X. C., pH-Triggered and Enhanced Simultaneous Photodynamic and Photothermal Therapy Guided by Photoacoustic and Photothermal Imaging. *Chem. Mater.* **2017**, *29*, 5216-5224. (b) Tang, Q. Y.; Si, W. L.; Huang, C. H.; Ding, K. K.; Huang, W.; Chen, P.; Zhang, Q.; Dong, X. C., An aza-BODIPY photosensitizer for photoacoustic and photothermal imaging guided dual modal cancer phototherapy. *J. Mater. Chem. B* **2017**, *5*, 1566-1573. (c) He, H.; Ji, S. S.; He, Y.; Zhu, A. J.; Zou, Y. L.; Deng, Y. B.; Ke, H. T.; Yang, H.; Zhao, Y. L.; Guo, Z. Q.; Chen, H. B., Photoconversion-Tunable Fluorophore Vesicles for Wavelength-Dependent Photoinduced Cancer Therapy. *Adv. Mater.* **2017**, *29*, 1606690. (d) Xu, Y. J.; Feng, T.; Yang, T. S.; Wei, H. J.; Yang, H. R.; Li, G.; Zhao, M. L.; Liu, S. J.; Huang, W.; Zhao, Q., Utilizing Intramolecular Photoinduced Electron Transfer to Enhance Photothermal Tumor Treatment of Aza-BODIPY-Based Near-Infrared Nanoparticles. *ACS Appl. Mater. Inter.* **2018**, *10*, 16299-16307. (e) Song, N.; Fu, L.; Liu, Y.; Li, Y. Y.; Chen, L.; Wang, X. Y.; Liu, S.; Xie, Z. G., Rational design of BODIPY organic nanoparticles for enhanced photodynamic/photothermal therapy. *Dyes Pigments* **2019**, *162*, 295-302. (f) Xi, D. M.; Xiao, M.; Cao, J. F.; Zhao, L. Y.; Xu, N.; Long, S. R.; Fan, J. L.; Shao, K.; Sun, W.; Yan, X. H.; Peng, X. J., NIR Light-Driving Barrier-Free Group Rotation in Nanoparticles with an 88.3% Photothermal Conversion Efficiency for Photothermal Therapy. *Adv. Mater.* **2020**, *32*, 1907855. (g) Jiang, Z. Y.; Zhang, C. L.; Wang, X. Q.; Yan, M.; Ling, Z. X.; Chen, Y. C.; Liu, Z. P., A Borondifluoride-Complex-Based Photothermal Agent with an 80 % Photothermal Conversion Efficiency for Photothermal Therapy in the NIR-II Window. *Angew. Chem. Int. Ed.* **2021**, *60*, 22376-22384. (h) Xiang, H. J.; Zhao, L. Z.; Yu, L. D.; Chen, H. Z.; Wei, C. Y.; Chen, Y.; Zhao, Y. L., Self-assembled organic nanomedicine enables ultrastable photo-to-heat converting theranostics in the second near-infrared biowindow. *Nat. Commun.* **2021**, *12*, 218. (i) Liu, B.; Jiao, J.; Xu, W.; Zhang, M.; Cui, P.; Guo, Z.; Deng, Y.; Chen, H.; Sun, W., Highly Efficient Far-Red/NIR-Absorbing Neutral Ir(III) Complex Micelles for Potent Photodynamic/Photothermal Therapy. *Adv. Mater.* **2021**, *33*, 2100795. (j) Su, Y.; Hu, Q.; Zhang, D.; Shen, Y.; Li, S.; Li, R.; Jiang,

X.-D.; Du, J., 1,7-Di-tert-butyl-Substituted aza-BODIPYs by Low-Barrier Rotation to Enhance a Photothermal-Photodynamic Effect. *Chem. Eur. J.* **2022**, *28*, e202103571.

10. (a) Liu, K. L.; Lalancette, R. A.; Jäkle, F., B-N Lewis Pair Functionalization of Anthracene: Structural Dynamics, Optoelectronic Properties, and O_2 Sensitization. *J. Am. Chem. Soc.* **2017**, *139*, 18170-18173. (b) Liu, K. L.; Lalancette, R. A.; Jäkle, F., Tuning the Structure and Electronic Properties of B-N Fused Dipyridylanthracene and Implications on the Self-Sensitized Reactivity with Singlet Oxygen. *J. Am. Chem. Soc.* **2019**, *141*, 7453-7462.

11. (a) Zhu, C. Z.; Guo, Z. H.; Mu, A. U.; Liu, Y.; Wheeler, S. E.; Fang, L., Low Band Gap Coplanar Conjugated Molecules Featuring Dynamic Intramolecular Lewis Acid-Base Coordination. *J. Org. Chem.* **2016**, *81*, 4347-4352. (b) Grandl, M.; Rudolf, B.; Sun, Y.; Bechtel, D. F.; Pierik, A. J.; Pammer, F., Intramolecular N -> B Coordination as a Stabilizing Scaffold for pi-Conjugated Radical Anions with Tunable Redox Potentials. *Organometallics* **2017**, *36*, 2527-2535. (c) Li, Y.; Meng, H.; Li, Y.; Pang, B.; Luo, G.; Huang, J., Adjusting the energy levels and bandgaps of conjugated polymers via Lewis acid–base reactions. *New J. Chem.* **2018**, *42*, 18961-18968. (d) Li, Y. C.; Meng, H. F.; Yan, D.; Li, Y. Q.; Pang, B.; Zhang, K.; Luo, G. G.; Huang, J. H.; Zhan, C. L., Synthesis of B <- N embedded indacenodithiophene chromophores and effects of bromine atoms on photophysical properties and energy levels. *Tetrahedron* **2018**, *74*, 4308-4314. (e) Morgan, M. M.; Nazari, M.; Pickl, T.; Rautiainen, J. M.; Tuononen, H. M.; Piers, W. E.; Welch, G. C.; Gelfand, B. S., Boron-nitrogen substituted dihydroindeno[1,2-b]fluorene derivatives as acceptors in organic solar cells. *Chem. Commun.* **2019**, *55*, 11095-11098. (f) Li, Y.; Meng, H.; Liu, T.; Xiao, Y.; Tang, Z.; Pang, B.; Li, Y.; Xiang, Y.; Zhang, G.; Lu, X.; Yu, G.; Yan, H.; Zhan, C.; Huang, J.; Yao, J., 8.78% Efficient All-Polymer Solar Cells Enabled by Polymer Acceptors Based on a B←N Embedded Electron-Deficient Unit. *Adv. Mater.* **2019**, *31*, 1904585. (g) Xiang, Y.; Meng, H.; Yao, Q.; Chang, Y.; Yu, H.; Guo, L.; Xue, Q.; Zhan, C.; Huang, J.; Chen, G., B ← N Bridged Polymer Acceptors with 900 nm Absorption Edges Enabling High-Performance All-Polymer Solar Cells. *Macromolecules* **2020**, *53*, 9529-9538. (h) Nguyen, T.; Hannah, T. J.; Piers, W. E.; Gelfand, B. S., Stable, π-conjugated radical anions of boron-nitrogen dihydroindeno[1,2-b]fluorenes. *Can. J. Chem.* **2022**, *DOI: 10.1139/cjc-2022-0039*.

12. Zhu, Y.; Rabindranath, A. R.; Beyerlein, T.; Tieke, B., Highly luminescent 1,4-diketo-3,6-diphenylpyrrolo[3,4-c]pyrrole(DPP-) based conjugated polymers prepared upon Suzuki coupling. *Macromolecules* **2007**, *40*, 6981-6989.

13. Iqbal, S. A.; Pahl, J.; Yuan, K.; Ingleson, M. J., Intramolecular (directed) electrophilic C-H borylation. *Chem. Soc. Rev.* **2020**, *49*, 4564-4591.

14. Frisch, M. J. *et al. Gaussian 09, Revision D.01, Gaussian, Inc., Wallingford CT, 2013.*

15. (a) Fischer, S., Correlation Function Approach to Radiationless Transitions. *J. Chem. Phys.* **1970**, *53*, 3195-3207. (b) Englman, R.; Jortner, J., The energy gap law for radiationless transitions in large molecules. *Molecular Physics* **1970**, *18*, 145-164.

16. Brega, V.; Yan, Y.; Thomas, S. W., Acenes beyond organic electronics: sensing of singlet oxygen and stimuli-responsive materials. *Org. Biomol. Chem.* **2020**, *18*, 9191-9209.

17. DeRosa, M. C.; Crutchley, R. J., Photosensitized singlet oxygen and its applications. *Coord. Chem. Rev.* **2002**, *233*, 351-371.